






Sub-millimetre light detection and ranging using perovskites

Amin Morteza Najarian^{1,4}  , Maral Vafaie^{1,4} , Andrew Johnston¹ , Tong Zhu¹, Mingyang Wei¹ ,
Makhsud I. Saidaminov^{1,3}, Yi Hou¹ , Sjoerd Hoogland¹ , F. Pelayo García de Arquer²  and
Edward H. Sargent¹  

Light detection and ranging (LiDAR) technology is an active remote-sensing system used in autonomous vehicles, machine vision and augmented reality. Improvements in the speed and signal-to-noise ratio of photodetectors are needed to meet these demanding ranging applications. Silicon electronics have been the principal option for LiDAR photodetectors in the range of 850–950 nm. However, its indirect bandgap leads to a low absorption coefficient in the near-infrared region, as well as a consequent trade-off between speed and efficiency. Here we report solution-processed lead-tin binary perovskite photodetectors that have an external quantum efficiency of 85% at 850 nm, dark current below 10^{-8} A cm^{-2} and response time faster than 100 ps. The devices are fabricated using self-limiting and self-reduced tin precursors that enable perovskite crystallization at the desired stoichiometry and prevent the formation of interfacial defects with the hole transport layer. The approach removes oxygen from the solution, converts Sn^{4+} to Sn^{2+} through comproportionation, and leaves neither metallic tin nor SnO_x residues. To illustrate the potential of these solution-processed perovskite photodetectors in LiDAR, we show that they can resolve sub-millimetre distances with a typical 50 μm standard deviation.

Light detection and ranging (LiDAR) technology measures the time for a short-pulsed light to scatter back from a target object and return to a detector^{1,2}. The measured time is converted to distance using the speed of light. By scanning illumination over a target scene, the system reconstructs a three-dimensional (3D) image¹. Photodetector characteristics play a central role in the resolution, accuracy and detection limits of the system. The ideal LiDAR photodetector should be fast and efficient with a low dark current at the operating bias. Two main LiDAR windows are employed: 850–950 and 1,330–1,550 nm. Current consumer electronics and automotive LiDAR systems mainly operate in the 850–950 nm region to minimize water absorbance and weather dependency (Supplementary Table 1). In the 850–950 nm window, silicon (Si) photodetectors have been the main approach due to their low cost and ease of system integration. However, there exists a trade-off between efficiency and speed in Si photodetectors (Fig. 1a)^{3,4}. Si has a weak absorption coefficient at LiDAR-relevant wavelengths ($\approx 2.7 \times 10^3 \text{ cm}^{-1}$ at 905 nm), which demands thick devices ($\approx 10 \mu\text{m}$) to absorb 90% of incident light in a single pass (Extended Data Fig. 1). However, to reach the 2 GHz bandwidth, the Si device thickness needs to be less than 3 μm . The indirect bandgap of Si, thus, limits its combined detection efficiency and speed (Fig. 1b). Solution-processed perovskites have a high optical absorption coefficient ($>10^4 \text{ cm}^{-1}$), high carrier mobility (tens of $\text{cm}^2 (\text{V s})^{-1}$) and long carrier diffusion length ($>1 \mu\text{m}$), making them promising candidates for fast photo-detection^{5–14}. Alloying lead-halide perovskites with tin extends the detection range into LiDAR-relevant wavelengths ($>850 \text{ nm}$)^{15–17}. The ratio of lead to tin also affects the crystallization process and film quality of the perovskite¹⁸. Calculations indicate that lead–tin (Pb–Sn) could potentially offer a route to unite speed and efficiency

(Fig. 1c; details in Extended Data Fig. 2). Modelling quantifies how the thickness of the photoactive layer determines the response time and external quantum efficiency (EQE) of the device. It is of interest to maximize the absorption coefficient using a high-quality crystalline dense film and to minimize the defect density in the film to permit the fast extraction of charges. A challenge in fabricating Pb–Sn perovskite devices is the susceptibility of Sn^{2+} to become oxidized in the precursor solution. The resulting Sn^{4+} species form trap states whose non-radiative recombination decreases the diffusion length in perovskite films, and deteriorates device performance^{15,16,19,20}. Several strategies have been developed to address tin oxidation, including the use of antioxidant additives such as SnF_2 , SnF_2 –pyrazine complex and hydroxybenzene sulfonic acid^{21–28}. In particular, the tin-powder-reduced precursor (TPRP) strategy has shown improved charge carrier diffusion lengths of $\approx 3 \mu\text{m}$ in Pb–Sn perovskite films¹⁶. The speed of a photodetector is dominated by the lowest of the mobility/thickness ratios looking across layers and carrier types throughout the structure. Accordingly, it is essential to use high-mobility hole transport layers (HTLs) and electron transport layers (ETLs) that achieve higher speed of photodetection. The high crystallinity of sol–gel NiO_x results in higher mobility ($\approx 10^{-3}$ to $10^{-1} \text{ cm}^2 (\text{V s})^{-1}$) compared with typical organic alternatives such as poly(3,4-ethylenedioxythiophene):poly(styrenesulfonate) (PEDOT:PSS) at $\approx 10^{-5}$ to $10^{-4} \text{ cm}^2 (\text{V s})^{-1}$ (refs. 29–32). It has been shown that the use of NiO_x as the HTL in pure-lead perovskite devices leads to better film quality—larger grain size, fewer pinholes and higher stability—compared with HTLs such as PEDOT:PSS (refs. 31,33–35). Despite these advantages of NiO_x , its use with Pb–Sn binary perovskites has been limited compared with devices that rely on PEDOT:PSS (refs. 15,16,33,36), and it has been shown that oxygen

¹The Edward S. Rogers Department of Electrical and Computer Engineering, University of Toronto, Toronto, Ontario, Canada. ²ICFO-Institut de Ciències Fotòniques, The Barcelona Institute of Science and Technology, Barcelona, Spain. ³Present address: Department of Chemistry, University of Victoria, Victoria, British Columbia, Canada. ⁴These authors contributed equally: Amin Morteza Najarian, Maral Vafaie. ✉e-mail: amin.morteza@utoronto.ca; ted.sargent@utoronto.ca

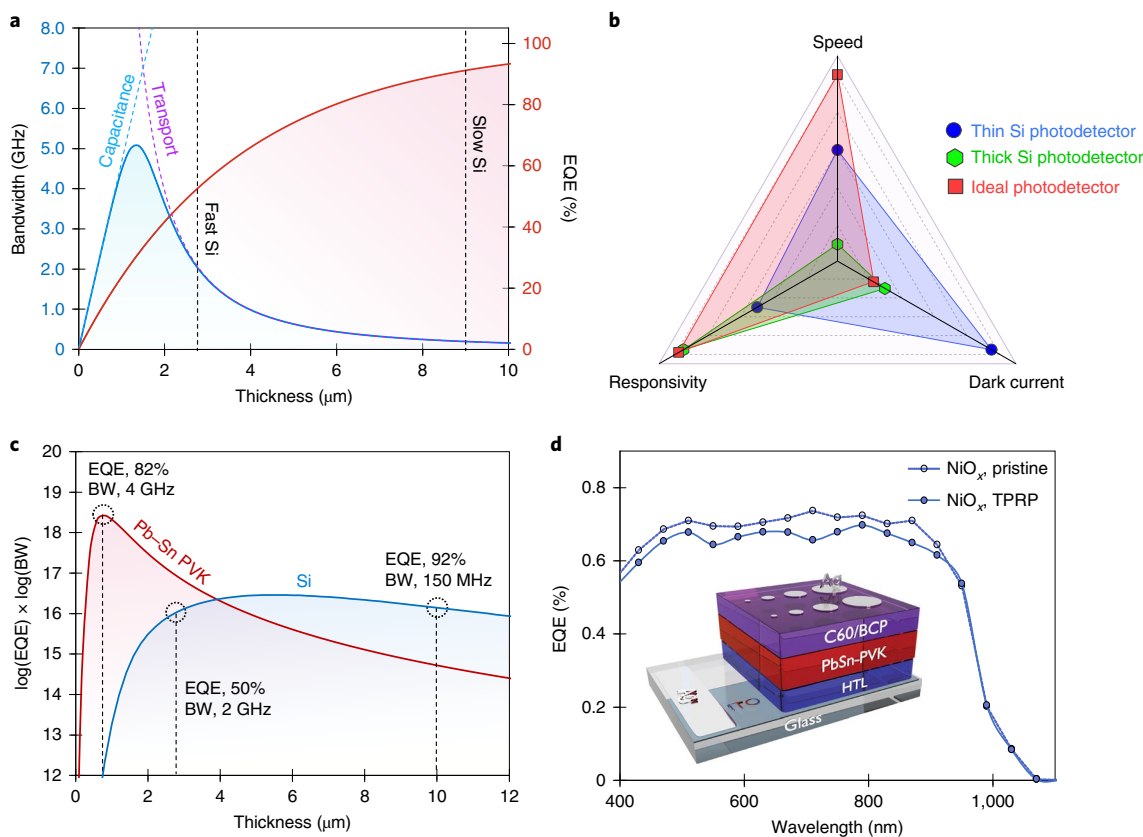


Fig. 1 | Si and Pb-Sn photodetectors. **a**, Performance modelling of Si PIN photodetector. Details and parameters of modelling are given in Methods and Extended Data Fig. 1. **b**, Comparison of fast and slow Si photodetector characteristics (Extended Data Table 1). Desirable characteristics for LiDAR photodetection are also shown. **c**, Modelling of combined speed-efficiency characteristics for Pb-Sn perovskites compared with Si. BW stands for bandwidth. The details and parameters for modelling are given in Extended Data Fig. 2. **d**, Effect of TPRP on the EQE of the photodetectors with NiO_x as the HTL. The inset shows the inverted architecture of the fabricated devices.

vacancies in metal oxide may contribute to tin oxidation in Pb-Sn perovskites^{37,38}. In this Article, we report a strategy to overcome the incompatibility of NiO_x and Pb-Sn perovskites, and create fast and efficient solution-processed photodetectors. We use self-limiting and self-reduced tin precursors. This approach removes oxygen from the solution, converts Sn^{4+} to Sn^{2+} through a comproportionation reaction and leaves no tin residue after filtration. This allows us to incorporate crystalline NiO_x as the HTL in Pb-Sn perovskite devices. The resulting devices exhibit an EQE of 85% at 850 nm, dark current below $10^{-8} \text{ A cm}^{-2}$ and response time faster than 100 ps. The combined efficiency and speed is more than two times higher than fast Si photodetectors and more than 100 times higher than previously reported solution-processed photodetectors. To illustrate the potential of this approach, we show that the solution-processed perovskite photodetectors can be used to resolve sub-millimetre distances with typical 50 μm standard deviations.

Pb-Sn photodetector with NiO_x HTL

We first fabricated photodetectors with an inverted planar architecture (indium tin oxide (ITO)/HTL/Pb-Sn/C60/bathocuproine (BCP)/Ag), where Pb-Sn is $\text{MA}_{0.3}\text{FA}_{0.7}\text{Pb}_{0.5}\text{Sn}_{0.5}\text{I}_3$ and the HTL is NiO_x or PEDOT:PSS as the control (Fig. 1d, inset). To limit the formation of Sn^{4+} vacancies in the perovskite film, we began by using a previously reported metallic tin precursor strategy¹⁶. We added 0.5 mg ml^{-1} Sn metallic microparticles (diameter, $<150 \mu\text{m}$) to the precursor solution, which we vigorously stirred for 10 min. We observed that the addition of metallic tin powder to the precursor solution decreased the EQE of the devices fabricated with NiO_x as

the HTL (Fig. 1d). This finding is in contrast to the improvement we saw in control PEDOT:PSS devices on the addition of Sn powder (Extended Data Fig. 3)¹⁶.

To explore the origins of the drop in EQE observed in NiO_x devices on incorporating metallic Sn powder into the precursor solution, we considered the possibility that residual Sn species may remain in the precursor solution following filtration—something that could arise due to an inhomogeneous particle distribution (Fig. 2a). To test this hypothesis, we dispersed metallic Sn powder ($<150 \mu\text{m}$) in a dimethylformamide:dimethyl sulfoxide (DMF:DMSO) (3:1 v/v) solution, stirred vigorously and analysed following filtration (0.22 μm filter). Inductively coupled plasma elemental analysis revealed the presence of Sn species in the solution after filtration (Supplementary Fig. 1). We then treated the NiO_x HTL with this solution and analysed its surface. Scanning electron microscopy (SEM) images of the NiO_x surface show a distribution of microparticles ($<200 \text{ nm}$) on the surface of NiO_x . Energy-dispersive X-ray (EDX) mapping demonstrates that these microparticles are Sn (Fig. 2b). Atomic force microscopy (AFM) imaging and X-ray photoelectron spectroscopy (XPS) analysis further support the presence of residual Sn on the surface of NiO_x (Supplementary Notes 2–4).

Compatible reducing strategy with NiO_x

The ideal reducing agent should provide a favourable balance among the surface area, reaction time and ease of removal, all with minimum probability of passing through the filtration step. The surface of the desired reducing agent should be of a form that exposes a high surface area to the solution and does not disintegrate into

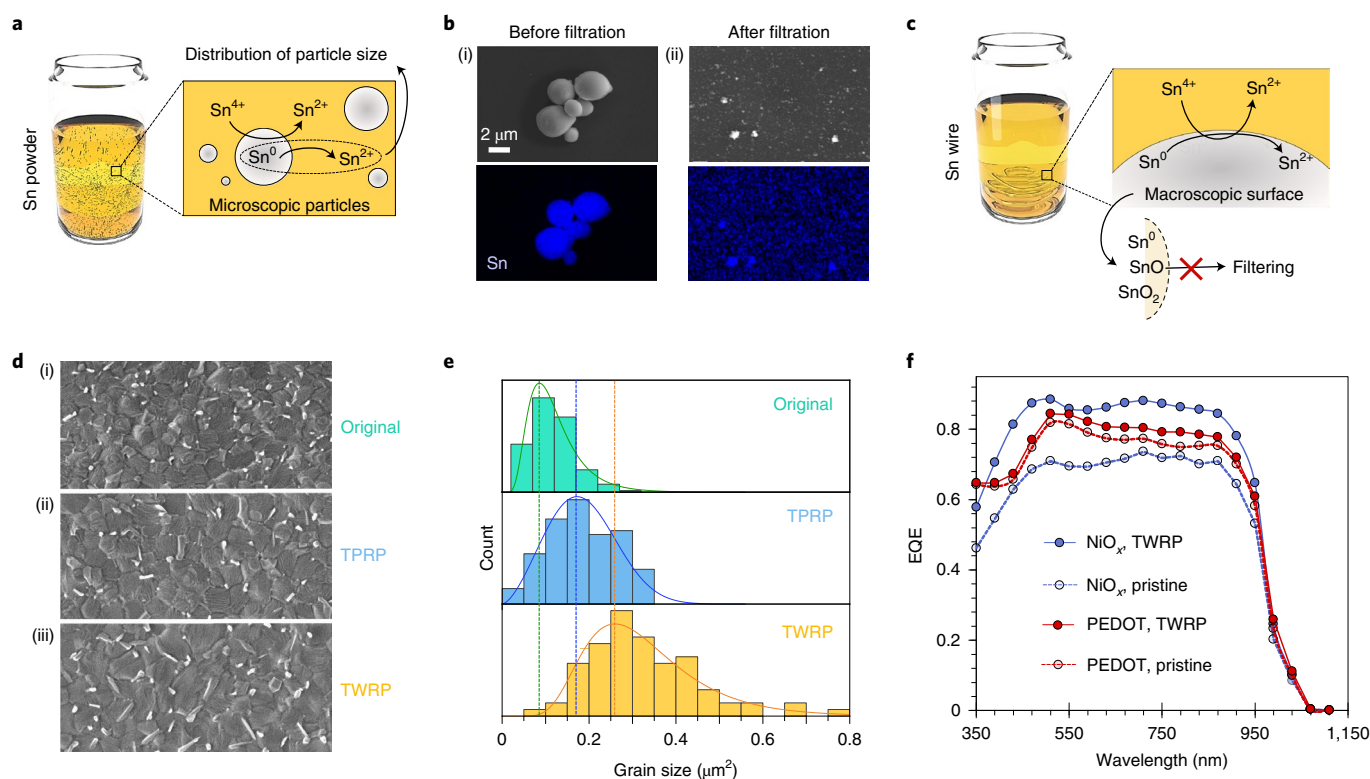


Fig. 2 | Reducing strategy for Sn precursor. **a**, Schematic of the Sn metallic powder reducing precursor process. **b**, SEM images and EDX Sn elemental mapping from the Si/NiO_x surface treated with Sn powder solution before filtration (i). The blue colour in the elemental map is assigned to elemental Sn (Supplementary Fig. 2 shows the EDX spectrum and analysis details). SEM images and EDX Sn elemental mapping from the Si/NiO_x surface treated with filtered Sn powder solution (ii). The blue colour in the elemental map is assigned to elemental Sn (Supplementary Fig. 3 shows the EDX spectrum and analysis details). **c**, Schematic showing the Sn metallic wire reducing precursor process. **d**, Surface SEM images of Pb-Sn perovskite spin coated on NiO_x with different reducing strategies: NiO_x-pristine precursor (i), NiO_x-TPRP (ii) and NiO_x-TWRP (iii). **e**, Histogram of the perovskite grain size for NiO_x/Pb-Sn perovskites in previously shown SEM images (Supplementary Fig. 5 shows a comparison with PEDOT:PSS). **f**, EQE of the devices using the TWRP strategy.

smaller pieces during long-duration reactions with oxygen. We posited that if we could simultaneously satisfy these requirements, the Sn surface would function as a self-limiting reducing agent for Sn⁴⁺, and that this would ensure that the time of reaction is not a critical process parameter: summarily, it would provide a wide process window in which high performance was achieved. Experimentally, we found that tin wire satisfied these requirements (Fig. 2c): the reactive macroscopic surface of Sn wire acts as a self-limiting reducing agent to convert unwanted Sn⁴⁺ to Sn²⁺, allowing Sn wire to react with oxygen in the precursor without leaving metallic Sn or SnO_x residue after filtration.

To explore the effect of reducing strategy (tin-wire-reduced precursor (TWRP) versus TPRP) on perovskite film growth, we compared the surface morphology of perovskite films on different HTLs. The SEM images of the surface show that the grain size of perovskite films grown on NiO_x is sensitive to the reducing strategy employed—in contrast to the case of PEDOT:PSS (Supplementary Note 1). This agrees with the following picture of the surface reactivity of NiO_x: unlike organic HTLs such as PEDOT:PSS, NiO_x—with its surface that includes exposed oxygen—is prone to react with residual metallic Sn, leading to the formation of an interfacial non-uniform and non-conformal carrier extraction barrier (Extended Data Fig. 4). The residual Sn species—whether metallic or oxide—present at the interface with NiO_x impede the nucleation and crystallization of perovskite and lead to a smaller grain size (Fig. 2d,e).

A Foster diagram shows that different forms of SnO_x have lower formation energies compared with NiO_x (Extended Data Fig. 4a).

Defects derived from this interface (NiO_x–perovskite) can be asymptomatic for d.c. photovoltaic operation under solar irradiance and yet be materially detrimental to the rapid charge extraction needed for time-of-flight (ToF) measurements^{39,40}. Density functional theory (DFT) simulations (based on the Perdew–Burke–Ernzerhof (PBE) functional within spin-polarized treatments) further support the negative impact of SnO_x formation on the performance of devices and the negative effect on energy-level alignment in devices (Extended Data Fig. 4b–g). This points to the importance of avoiding the presence of Sn residual species on NiO_x as they are deleterious to the crystallization kinetics of Pb–Sn perovskites and work against the energy-level alignment needed within p–i–n (PIN) devices (Supplementary Note 2).

When we used the TWRP strategy, we no longer saw negative impacts akin to those observed when extra clusters of Sn species were present in the perovskite precursor mix (Fig. 2d,e). Figure 2f shows that the NiO_x HTL with the TWRP results yields an EQE of ≈ 85%, which is higher than the control PEDOT:PSS devices. NiO_x devices show a lower dark current compared with PEDOT:PSS, achieving values below 10^{−8} A cm^{−2} (Extended Data Fig. 3c). The representative dark-current curves for PEDOT:PSS and NiO_x are shown in Extended Data Fig. 3b.

Pb–Sn photodetector performance

We compare these results with those of the best near-infrared solution-processed photodetectors across organics, quantum dots and perovskites. Figure 3a shows the EQE versus dark current in the highest-performing previously reported detectors having a

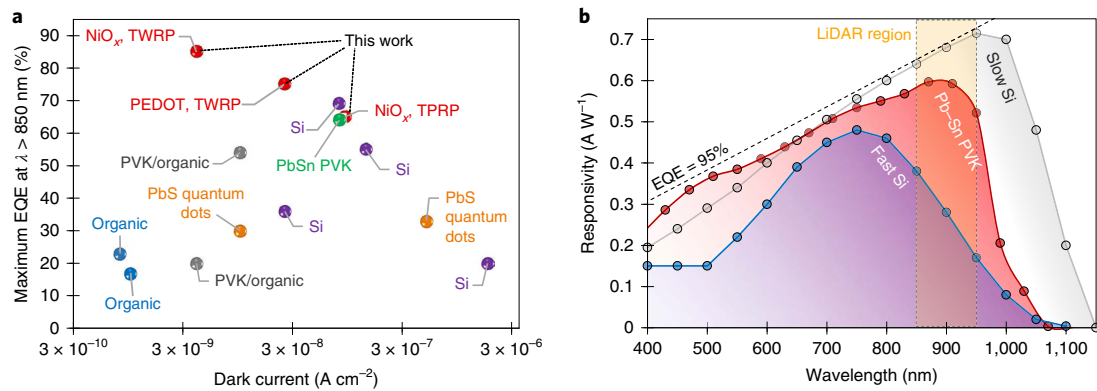


Fig. 3 | Performance of Pb-Sn photodetectors. **a**, Plot of the maximum EQE for wavelengths >850 nm versus the minimum dark current at the operating bias. For devices operating without external bias, the dark current at 50 mV is plotted (Extended Data Fig. 5a and Extended Data Table 2). **b**, Responsivity of our Pb-Sn photodetector compared with commercial Si fast and slow photodetectors. Details of commercial fast and slow photodetectors from different companies are given in Extended Data Fig. 5b and Extended Data Table 1.

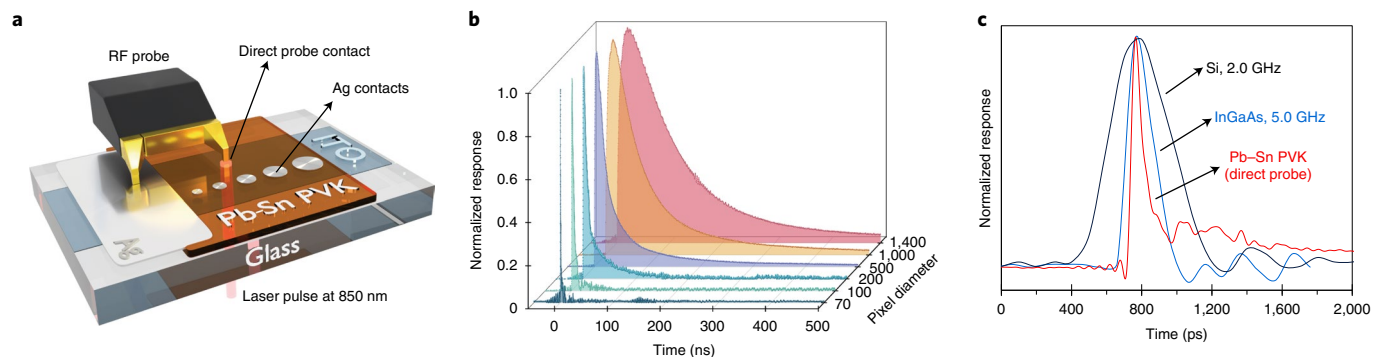


Fig. 4 | Speed measurements for Pb-Sn devices. **a**, Schematic illustrating the TPC measurements. An RF probe with a two-point contact (signal-ground) is used to make a connection with the bottom ITO electrode and top Ag electrode with different pixel areas. Direct contact of the RF probe with the surface of the ETL (without an Ag electrode) leads to a working device with a small area ($<10 \times 10 \mu\text{m}^2$). **b**, A 3D plot showing the normalized response versus time for different pixel sizes. The Y axis is the diameter of the pixel in micrometres. **c**, Comparison of Pb-Sn response time (with direct probe contact) with commercialized 2.0 GHz Si and 5.0 GHz GaAs photodetector. Extended Data Fig. 5c and Extended Data Table 1 show the detailed characteristics of the shown commercial photodetector.

detection range of >850 nm. Extended Data Table 1 is limited to reports that include the measured speed of photodetection.

Integrating the TWRP strategy for Pb-Sn perovskites with the NiO $_x$ HTL offers values of EQE that are 20 absolute percentage points higher than the highest-performing previously reported solution-processed photodetectors at LiDAR-relevant wavelengths (Fig. 3a). For Si, high speed can only be attained with thin active layers, which results in higher dark currents and lower EQE values. Figure 3b shows the overlay of the Pb-Sn photodetector responsivity spectra with high- and low-speed Si photodetectors. The quantum efficiency of slow commercial Si photodetectors approaches $\approx 93\%$ at 905 nm, but these values are reduced in fast Si photodetectors (EQE $< 50\%$). Direct noise measurements in a wide frequency range using a signal analyser show the equivalent noise level of $100 \text{ fA Hz}^{-0.5}$ for Pb-Sn perovskite photodetectors. Using the responsivity reported in Fig. 3b, we obtain a specific detectivity of $\approx 1.5 \times 10^{12} \text{ cm Hz}^{1/2} \text{ W}^{-1}$ at 905 nm (Supplementary Fig. 8).

We carried out stability measurements, under ambient conditions, on encapsulated Pb-Sn photodetectors that use NiO $_x$ as the HTL. Devices with the NiO $_x$ HTL retained 95% of their photoresponse after 10 h of continuous illumination (Supplementary Fig. 9).

We compare the best-reported stability for photodetectors operating at LiDAR-relevant wavelengths (Supplementary Table 4).

We used transient photocurrent (TPC; Fig. 4a) to characterize the response time of Pb-Sn perovskite photodetectors. A two-point contact (signal-ground) radio-frequency (RF) probe with a pitch of $1,000 \mu\text{m}$ was used to contact the bottom ITO electrode and top Ag electrode, whose size defines the detection area. Figure 4b shows the TPC results for different pixel sizes. An analysis of the response time versus pixel area (Extended Data Fig. 6) reveals that the response time decreases with the pixel area and does not plateau even at the smallest pixel area of $\approx 0.005 \text{ mm}^2$. Considering a dielectric constant of $\epsilon \approx 51$, estimated via impedance spectroscopy (Extended Data Fig. 7), we conclude that the geometrical capacitance of the Pb-Sn perovskite plays an important role in determining speed (Extended Data Fig. 6): even at the smallest pixel area reported here, we had not yet reached transport-limited performance, and thus, we were motivated to develop a strategy to circumvent the geometrical capacitance limitation.

Direct contact of the signal side of the RF probe with the ETL surface of the device resulted in a contact area of approximately $10 \times 10 \mu\text{m}^2$. This strategy enabled us to reach a full-width at

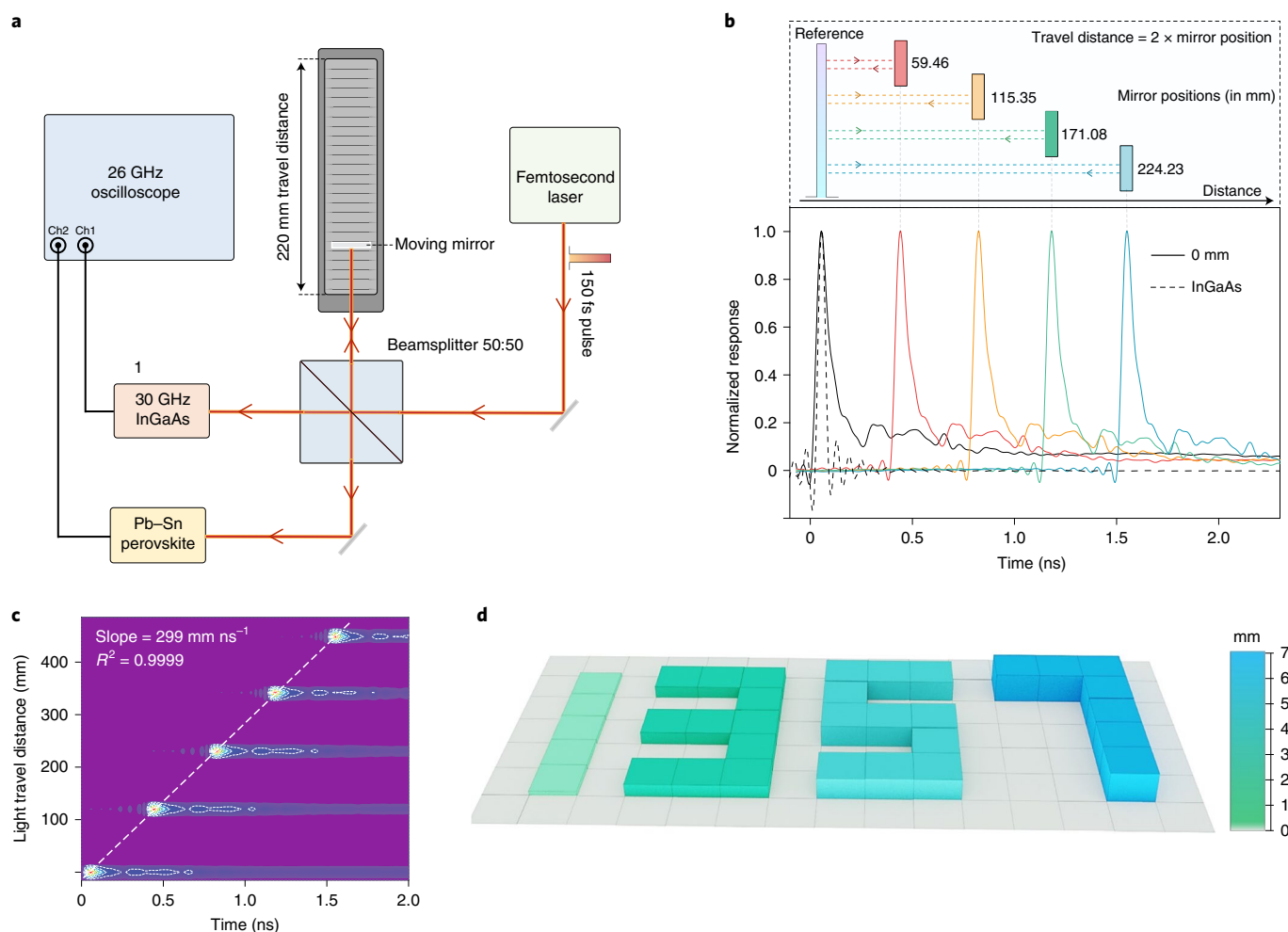


Fig. 5 | ToF measurements. **a**, Schematic of the ToF measurement. Michelson interferometer configuration is used to trigger the oscilloscope and remove jitter of the femtosecond laser. **b**, Response of the Pb-Sn photodetector at the indicated position of the moving mirror. The response of the InGaAs detector is shown as a reference (fixed position). **c**, Contour plot of the data shown in **a** versus the travel distance of light with respect to the reference. The slope of the line determines the measured speed of light. **d**, A 3D visualization of the estimated depth using the peak position of the Pb-Sn photodetector response. Each pixel is an individual measurement, and the depth is controlled and programmed by a moving mirror on a motorized stage (Extended Data Fig. 8).

half-maximum response time of 100 ps. Figure 4c shows a comparison between the response time of the Pb-Sn photodetector with the direct probe contact and a commercial fast Si and GaAs photodiode (Extended Data Table 2 provides the details of the commercial photodetector). We note that the data shown in Fig. 4c are not for the same detector area; however, a Si photodetector operates in a transport-limited regime and is therefore not limited by geometrical capacitance. Consequently, a decrease in the Si detector size does not lead to a faster response time (Extended Data Fig. 6). As evident from Fig. 4c, the Pb-Sn photodetector offers a narrower full-width at half-maximum value and a comparable fall time (90% to 10%) to 5.0 GHz GaAs photodetector.

LiDAR with Pb-Sn perovskites

We developed a system to apply the photodetectors developed here in the LiDAR-based estimation of the distance of objects. We used a Michelson interferometer configuration in a ToF setup (Fig. 5a). Using a beamsplitter, we referenced the pulsed light to a commercial InGaAs at a fixed position. Figure 5b shows the response of a Pb-Sn photodetector at different positions of the moving mirror of the interferometer. The contour graph (Fig. 5c) shows the light travel distance versus time, and the slope of the line gives the speed of light at 299 mm ns^{-1} . To visualize the accuracy of the depth estimation

using the Pb-Sn perovskite photodetector, we moved the mirror based on a predefined map and estimated the distance by the same ToF setup shown in Fig. 5a (Extended Data Fig. 8). We then reconstructed a 3D image using these individual measurements (Fig. 5d).

Conclusions

PIN photodetectors are used in short-range LiDAR applications. Our Pb-Sn devices meet the specifications in terms of EQE, response time and low dark current that make them competitive in these short-range high-accuracy LiDAR applications. However, to expand its applicability to long-range detection, multiplication will be needed to detect small signals (Supplementary Table 2). The flexibility of solution-processed perovskites may also allow incorporation into an avalanche amplification structure, and will be an important subject of further investigation.

Methods

Materials and preparation. Unless indicated otherwise, all the materials were purchased from Sigma-Aldrich and used as received. Formamidineum iodide (FAI), methylammonium iodide (MAI), PbI_2 and SnI_2 were acquired from Great Cell and Alfa Aesar. A perovskite precursor solution (1.7 M) was prepared by mixing the precursors based on the molar ratio of $\text{FA}_{0.7}\text{MA}_{0.30}\text{Pb}_{0.5}\text{Sn}_{0.5}\text{I}_3$ in the mixture of DMF:DMSO (3:1 v/v). The SnF_2 precursor was added by 10 mol% relative to the SnI_2 amount. We noticed that it is important to preheat the precursor glass vial at

100 °C for 15 min. The obtained mixture was prepared inside the nitrogen glovebox. After stirring at room temperature for 2 h, the solution was filtered through a 0.45 µm polytetrafluoroethylene (PTFE) syringe filter. For the TPRP samples, tin powders (5 mg ml⁻¹) were added, stirred at room temperature for 10 min and filtered using a 0.45 µm PTFE syringe filter before use. For the TWRP samples, a few-centimetre-long Sn wire (99.999%, MilliporeSigma; 0.5 mm diameter) was dropped inside the solution, which was stirred for an additional hour before filtration. We noticed that expanding the time of this reaction to more than one hour does not affect the performance. A 1.0 M NiO_x solution was prepared by the initial mixing of Ni(NO₃)₂·6H₂O with ethylene glycol (anhydrous, 99.8%) followed by the addition of ethylenediamine (>99.0%) in a molar ratio of 1.1:1.0 with respect to the Ni precursor. The solution was stirred overnight, followed by its dilution to the favourable concentration of 0.23 M. The solution was filtered using a 0.45 µm polyvinylidene fluoride (PVDF) syringe filter before deposition.

Device fabrication. For NiO_x films, the as-prepared NiO_x solution was spin coated on a precleaned ITO substrate at 4,000 rpm for 90 s and annealed at 300 °C on a hotplate for 1 h in ambient air. We tested the ultraviolet illumination post-treatment, but it had a negative impact on the device performance. For PEDOT:PSS films, the solution (Xi'an PLT) was spin coated on the substrates at 4,000 rpm for 30 s followed by annealing at 150 °C on a hotplate for 30 min in ambient air. The substrates were transferred to a nitrogen glovebox after annealing. We also diluted the PEDOT:PSS with methanol in a different ratio, but we did not observe any statistical and reproducible difference on the EQE of the devices. For the deposition of perovskite films, the as-prepared precursor solution was spin coated in a two-step procedure: (1) 1,000 rpm for 10 s with a ramping speed of 200 rpm s⁻¹ and (2) 4,000 rpm for 50 s with an acceleration of 1,000 rpm s⁻¹. During the second spin-coating step, 250 µl chlorobenzene (anhydrous, 99.8%) was dynamically dispensed on the substrate at 25 s before the end of the procedure. Immediately after deposition, the substrates with PEDOT:PSS were annealed on a hotplate at 100 °C for 10 min. The perovskite films deposited on NiO_x as the HTL were annealed on a hotplate in two steps: first at 50 °C for 5 min and then at 85 °C for another 5 min. C₆₀ (Xi'an PLT), BCP (TCI Chemicals) and Ag electrode were deposited in an Angstrom thermal evaporation system to form 20 nm C₆₀, 7 nm BCP and 250 nm Ag on top of the perovskite layer, respectively.

Device characterization. Dark current–voltage (*J*–*V*) characteristics were measured using a Keithley 2400 sourcemeter by scanning the bias between –0.3 and 0.3 V for pixels with an active area of 0.1 mm². The EQE spectra were measured using a Newport QUANTX-300 system without applying any external bias. Both *J*–*V* and EQE measurements were carried out under a constant flow of nitrogen. The TPC measurement was performed with a 26 GHz signal–ground RF probe (T26A, MPI Corporation) with a 1,000 µm pitch. Using a fast SMA cable, the probe was directly connected to the 50 Ω input of an oscilloscope (16 GHz Agilent DSAX91604A Infiniium). Then, 150 fs laser pulses at a 5 kHz repetition rate were produced using a regeneratively amplified Yb:KGW laser (PHAROS, Light Conversion) with an average power of ≈ 100 µW mm⁻² after focusing the light to a beam area of ≈ 0.008 mm². To test the response time in the low-power range, we used a gigahertz amplifier (FEMTO HSA-X-I-2-40) with a fixed gain at 40 dB. The time response with and without the usage of the amplifier is shown in Supplementary Fig. 11. We did not observe differences in the response time of the devices when we varied the average power (1–1,000 µW mm⁻² at the detector level) of the femtosecond laser. To test the validity of the TPC setup, we also report the response of commercial photodetectors—30 GHz InGaAs (Fig. 5a), 2 GHz Si (Fig. 4c) and 5 GHz InGaAs (Fig. 3c). We report these using the same power, light duration and conditions used in perovskite (PVK) photodetector studies. The measured response time matches the specifications provided by the vendors. The experiments were carried out at 850 nm. A 12 GHz bias tee was connected to a Keithley 2602 instrument in the circuit. The electrical output signal from the femtosecond laser system was used to trigger the oscilloscope.

Testing the presence of residual Sn on the surface of NiO_x. We explored the presence of Sn powder after filtration on the surface of NiO_x films via AFM, SEM/EDX and XPS analyses. Samples were prepared with the same procedure as perovskite film fabrication, excluding the usage of perovskite precursors, as discussed earlier. The NiO_x films were formed on precleaned Si substrates to avoid the reading of the Sn signal in elemental analysis from ITO substrates. Solutions containing Sn powder were prepared by dispersing an extra amount of Sn powder in the mixture of DMF:DMSO followed by 10–15 min vigorous stirring (Supplementary Fig. 1). The solution was filtered through a 0.22 µm PTFE syringe filter (the same filter was used for the filtration of the perovskite precursor solution). The surface of the Si/NiO_x samples was treated with unfiltered and filtered solutions followed by annealing on a hotplate at 85 °C. To remove any residue from the surface, the samples were washed two times by spin coating the DMF:DMSO solvent mixture. The XPS samples were prepared using the same procedure but inside a nitrogen glovebox.

SEM/EDX mapping measurement. High-resolution SEM images were acquired using a Hitachi SU5000 instrument. The samples were prepared by depositing

Pb–Sn PVK on top of NiO_x/ITO and PEDOT/ITO substrates using the same condition as device fabrication. To map the elemental composition of certain SEM samples, EDX analysis was carried out using a Bruker EDX detector. The EDX measurement conditions were set in the range of 8–15 kV.

AFM. The film morphology was characterized using an AFM instrument (Asylum Research Cypher) operated in the a.c. tapping mode equipped with AC240TM-R3 probes (resonant frequency, 70 kHz; spring constant, 2 N m⁻¹). To obtain high-quality images, areas of 5 × 5 µm² were probed using 1 Hz scanning rate and 1,024 lines per point.

XPS. XPS analysis was performed using an ESCALAB 250Xi system (Thermo Fisher Scientific) with an Al Kα source and a 500 µm X-ray spot size. A beam of low-energy argon-ion clusters (3 keV) was vertically employed on a raster area of 1 mm².

EQE measurements. The responsivity and quantum efficiency of the devices were measured using a QUANTX-300 Newport measurement system. No external bias was applied, and the measurements were taken under a constant nitrogen flow. A standard calibrated Si/Ge reference detector (BD005, Newport) was used to provide values of quantum efficiency/responsivity over the wavelength range from 350 to 1,800 nm. Calibration was conducted before each set of measurements to create the reference values. A Si photovoltaic test cell was used to further validate the calibration procedure.

Impedance spectroscopy. Impedance spectroscopy is employed to estimate the dielectric constant of the Pb–Sn perovskite film. For this purpose, the fabricated device with PEDOT:PSS as the HTL is connected to an Autolab potentiostat/galvanostat module. An a.c. voltage perturbation of 20 mV is applied as the device is kept in the dark and short-circuit conditions. The impedance spectra are collected as the frequency scans from 1 Hz to 1 MHz (Extended Data Fig. 7a). The capacitance component *C* is calculated based on the relationship with impedance *Z* and angular frequency ω (ref. 41).

$$C = \frac{1}{(\omega Z)}$$

Plotting capacitance versus frequency (Extended Data Fig. 7b) exhibits a typical behaviour consisting of two plateaus when decreasing the frequency from 1 MHz to 1 Hz (ref. 42). The plateau located in the low-frequency range (~1 Hz) is associated with the accumulated charges at interfaces; the high-frequency part of the spectra (>1 kHz), on the other hand, represents the geometrical capacitance *C_g* corresponding to the dielectric response of the perovskite layer. Accordingly, the dielectric response (ϵ) of the perovskite layer can be calculated as

$$C_g = \frac{A\epsilon\epsilon_0}{d},$$

where ϵ_0 is the permittivity of free space, ϵ is the dielectric constant of the material, *d* is the thickness of the light-absorbing perovskite layer and *A* is the overlapping area between the two electrodes (*d* = 500 nm and *A* = 0.1 cm²)⁴³. To calculate the accurate value of *C_g*, a proper equivalent-circuit representative of the resistive and capacitive responses of the system should be fitted (Extended Data Fig. 7a,b, solid lines). Based on previous studies on perovskite solar cells⁴⁴, the equivalent circuit of choice is a modified version of the standard Randles circuit (Extended Data Fig. 7c), which delivers the best fit to the measured data. Fitting results, as well as the calculated dielectric constant, are tabulated in Extended Data Fig. 7d. The obtained value for the dielectric constant is in good agreement with the values reported for metal halide perovskites^{44,45}.

Noise measurement. Noise spectra have been acquired using a signal analyser (N9010A, Agilent) combined with a low-noise transimpedance preamplifier at 10⁷ V A⁻¹ gain (FEMTO, DHPA-100). The devices (area, 0.1 cm²) were operated under short-circuit and dark conditions.

LiDAR demo. For distance estimation, we used the same equipment and arrangement as the TPC setup to measure the time response, but we split the femtosecond laser using a 50:50 beamsplitter before using one-half of the split beam to illuminate the sample. The other part was used as a reference and was directed to a 30 GHz InGaAs photodetector (Thorlabs, DXM30BF). The oscilloscope was triggered by the photodetector signal connected to channel 2; it was also used as a reference with a fixed position. The second part of the light was directed to the mirror (beam area, 10 mm²) installed on the linear stage (Newport) with a maximum travel distance of ≈ 250 mm. When we used a 40 dB electrical amplifier, we were able to reduce the energy density of light at the object (mirror) to 2 × 10⁻¹¹ J cm⁻² as the signal-to-noise ratio was maintained above 5. The reflected light from the mirror was directed to the Pb–Sn photodetector and focused on the corresponding pixel with a series of eyeball lenses. For the demo, a motorized stage moved the mirror based on the map provided in Extended Data Fig. 8. Note that there is no *X*–*Y* movement and just the depth (*Z*) has been scanned. The 3D image

was reconstructed using the estimated travel distance by considering the peak position of the response and speed of light (Extended Data Fig. 8).

DFT calculation. The DFT calculations were performed using the FHI-aims all-electron code^{46–48}. The default numerical settings, referred to as ‘tight’ in FHI-aims, were used. Spin-polarized treatment for Ni atom was incorporated into all the calculated electronic properties and geometry relaxation. More specifically, NiO in all the structures (that is, bulk and superlattice calculations) adopted a type-II antiferromagnetic phase (that is, the spin-ordering vector is along the [111] direction). Local minimum-energy geometries of the Born–Oppenheimer surface were obtained with residual total energy gradients below $1 \times 10^{-2} \text{ eV \AA}^{-1}$ for atomic positions by using the PBE generalized gradient approximation functional. To analyse the band alignment of NiO/SnO and NiO/SnO₂, we adopted the method described earlier^{49–56}, in which the valence-band offset, ΔE_{VBM} is defined as

$$\Delta E_{\text{VBM}}[\text{NiO/SnO, SnO}_2] = (E_{\text{VBM}}^{\text{SnO/SnO}_2} - E_{\text{VBM}}^{\text{NiO}}) + \Delta V,$$

where $E_{\text{VBM}}^{\text{SnO/SnO}_2}$ ($E_{\text{VBM}}^{\text{NiO}}$) represents the position of the valence-band maximum (VBM) with respect to the average electrostatic potential in materials SnO/SnO₂ (NiO), and ΔV represents the potential alignment term obtained from the superlattice calculations (Extended Data Fig. 4). According to another study⁴, the $E_{\text{VBM}}^{\text{SnO/SnO}_2}$ ($E_{\text{VBM}}^{\text{NiO}}$) value is obtained by using a hybrid functional (HSE06), and the potential alignment term ΔV is calculated based on a fully relaxed superlattice by the PBE generalized gradient approximation functional (which is proved to give similar accuracy as HSE06, but within less computational cost). More specifically, instead of using the plane-average electrostatic potential to calculate ΔV , the electronic potential at the cores of oxygen atoms is used to eliminate the oscillations caused by the ionic cores (Extended Data Fig. 4b,c). The final band-alignment schematic plots are shown in Extended Data Fig. 4d,e.

Photodetector performance modelling. The temporal response (τ_{r}) of a photodetector is modelled based on its dependence on the carrier transient time (τ_{tr}), RC-limited time response (τ_{RC}) and diffusion time (τ_{diff}) as follows.

$$\tau_{\text{r}} = \sqrt{(\tau_{\text{tr}})^2 + (\tau_{\text{RC}})^2 + (\tau_{\text{diff}})^2} \quad (1)$$

The transient time is predicted based on the bias across the sample (V), mobility (μ) and film thickness (d).

$$\tau_{\text{tr}} = \frac{d^2}{\mu V} \quad (2)$$

The RC constant is another limitation to the photodetector speed as it defines the time it takes to charge/discharge the capacitors in the electrical circuit. Assuming a simple parallel-plate capacitance model, the equation is derived as below.

$$\tau_{\text{RC}} = 2.2RC = \frac{2.2RA\epsilon\epsilon_0}{d} \quad (3)$$

In the calculations, we have assumed that the diffusion time is negligible compared with drift and RC time constant, and the field is linear across the sample thickness.

Finally, the -3 dB bandwidth of a photodetector relates to the temporal response according to the following equation.

$$\text{BW} = 0.35/\sqrt{\left(\frac{2.2AR\epsilon\epsilon_0}{d}\right)^2 + \left(\frac{d^2}{\mu V}\right)^2} \quad (4)$$

Using the Beer–Lambert law and assuming that the reflectance is negligible, the absorbance of a material relates to its transmittance (T), absorption coefficient (α) and thickness (d) as below.

$$A = 1 - T = 1 - e^{-\alpha d} \quad (5)$$

The EQE is defined as the number of photogenerated carriers divided by the number of incident photons. The internal quantum efficiency (IQE) is defined as the ratio of the photogenerated carriers to the number of absorbed photons. Therefore, the division of these two quantities gives the percentage of absorbed photons (A). As a result, the following equation describes the relationship between the EQE and thickness of the photoactive layer.

$$\text{EQE} = \text{IQE} \times (1 - e^{-\alpha d}) \quad (6)$$

In this paper, for comparison between Si and Pb–Sn, it is assumed that IQE at 905 nm is equal to unity for both architectures (IQE = 1.0). We note that assuming IQE of 0.7 to 1.0 does not change the conclusions of the model regarding the performance advance of Pb–Sn-perovskites over Si (Supplementary Fig. 10). To improve readability, a table containing the raw data obtained from device modelling is provided in Supplementary Table 3. In each column, we have referred to the equation listed in Methods.

Data availability

The datasets generated during and/or analysed during the current study are available from the corresponding author on reasonable request.

Received: 1 September 2021; Accepted: 17 June 2022;

Published online: 25 July 2022

References

- Royo, S. & Ballesta-García, M. An overview of LiDAR imaging systems for autonomous vehicles. *Appl. Sci.* **9**, 4093 (2019).
- Behroozpour, B., Sandborn, P. A. M., Wu, M. C. & Boser, B. E. LiDAR system architectures and circuits. *IEEE Commun. Mag.* **55**, 135–142 (2017).
- Yatsui, T. et al. Enhanced photo-sensitivity in a Si photodetector using a near-field assisted excitation. *Commun. Phys.* **2**, 62 (2019).
- Noffsinger, J., Kioupakis, E., Walle, C. G., Van de, Louie, S. G. & Cohen, M. L. Phonon-assisted optical absorption in silicon from first principles. *Phys. Rev. Lett.* **108**, 167402 (2012).
- Meredith, P. & Armin, A. Scaling of next generation solution processed organic and perovskite solar cells. *Nat. Commun.* **9**, 5261 (2018).
- Fu, F. et al. High-efficiency inverted semi-transparent planar perovskite solar cells in substrate configuration. *Nat. Energy* **2**, 16190 (2016).
- Kim, Y. C. et al. Printable organometallic perovskite enables large-area, low-dose X-ray imaging. *Nature* **550**, 87–91 (2017).
- Saliba, M., Correa-Baena, J.-P., Grätzel, M., Hagfeldt, A. & Abate, A. Perovskite solar cells: from the atomic level to film quality and device performance. *Angew. Chem. Int. Ed.* **57**, 2554–2569 (2018).
- García De Arquer, F. P., Armin, A., Meredith, P. & Sargent, E. H. Solution-processed semiconductors for next-generation photodetectors. *Nat. Rev. Mater.* **2**, 16100 (2017).
- Zhou, J. et al. Lead-free perovskite derivative Cs₂SnCl_{6-x}Br_x single crystals for narrowband photodetectors. *Adv. Opt. Mater.* **7**, 1900139 (2019).
- Stranks, S. D. et al. Electron-hole diffusion lengths exceeding 1 micrometer in an organometal trihalide perovskite absorber. *Science* **342**, 341–344 (2013).
- Fu, Y. et al. Metal halide perovskite nanostructures for optoelectronic applications and the study of physical properties. *Nat. Rev. Mater.* **4**, 169–188 (2019).
- Correa-Baena, J.-P. et al. Promises and challenges of perovskite solar cells. *Science* **358**, 739–744 (2017).
- Dou, L. et al. Solution-processed hybrid perovskite photodetectors with high detectivity. *Nat. Commun.* **5**, 5404 (2014).
- Werner, J. et al. Improving low-bandgap tin–lead perovskite solar cells via contact engineering and gas quench processing. *ACS Energy Lett.* **5**, 1215–1223 (2020).
- Lin, R. et al. Monolithic all-perovskite tandem solar cells with 24.8% efficiency exploiting comproportionation to suppress Sn(II) oxidation in precursor ink. *Nat. Energy* **4**, 864–873 (2019).
- Prasanna, R. et al. Design of low bandgap tin–lead halide perovskite solar cells to achieve thermal, atmospheric and operational stability. *Nat. Energy* **4**, 939–947 (2019).
- Lee, S., Ha, T. J. & Kang, D. W. Mixed-halide Pb–Sn binary perovskite films with various Sn-content for Pb-reduced solar cells. *Mater. Lett.* **227**, 311–314 (2018).
- Jiang, T. et al. Realizing high efficiency over 20% of low-bandgap Pb–Sn-alloyed perovskite solar cells by in situ reduction of Sn⁴⁺. *Sol. RRL* **4**, 1900467 (2020).
- Ghimire, N. et al. Mitigating open-circuit voltage loss in Pb–Sn low-bandgap perovskite solar cells via additive engineering. *ACS Appl. Energy Mater.* **4**, 1731–1742 (2021).
- Tai, Q. et al. Antioxidant grain passivation for air-stable tin-based perovskite solar cells. *Angew. Chem. Int. Ed.* **58**, 806–810 (2019).
- Ma, L. et al. Carrier diffusion lengths of over 500 nm in lead-free perovskite CH₃NH₃SnI₃ films. *J. Am. Chem. Soc.* **138**, 14750–14755 (2016).
- Lee, S. J. et al. Fabrication of efficient formamidinium tin iodide perovskite solar cells through SnF₂–pyrazine complex. *J. Am. Chem. Soc.* **138**, 3974–3977 (2016).
- Liao, W. et al. Lead-free inverted planar formamidinium tin triiodide perovskite solar cells achieving power conversion efficiencies up to 6.22%. *Adv. Mater.* **28**, 9333–9340 (2016).
- Konstantakou, M. & Stergiopoulos, T. A critical review on tin halide perovskite solar cells. *J. Mater. Chem. A* **5**, 11518–11549 (2017).
- Ke, W. et al. Ethylenediammonium-based ‘hollow’ Pb/Sn perovskites with ideal band gap yield solar cells with higher efficiency and stability. *J. Am. Chem. Soc.* **141**, 8627–8637 (2019).
- Xiao, K. et al. All-perovskite tandem solar cells with 24.2% certified efficiency and area over 1 cm² using surface-anchoring zwitterionic antioxidant. *Nat. Energy* **5**, 870–880 (2020).
- Gu, F. et al. Improving performance of lead-free formamidinium tin triiodide perovskite solar cells by tin source purification. *Sol. RRL* **2**, 1800136 (2018).

29. Zhang, J. et al. Solution-processed Sr-doped NiO_x as hole transport layer for efficient and stable perovskite solar cells. *Sol. Energy* **174**, 1133–1141 (2018).
30. Liu, A. et al. Hole mobility modulation of solution-processed nickel oxide thin-film transistor based on high-*k* dielectric. *Appl. Phys. Lett.* **108**, 233506 (2016).
31. Kung, P.-K. et al. A review of inorganic hole transport materials for perovskite solar cells. *Adv. Mater. Interfaces* **5**, 1800882 (2018).
32. Chang, C.-C., Tao, J.-H., Tsai, C.-E., Cheng, Y.-J. & Hsu, C.-S. Cross-linked triarylamine-based hole-transporting layer for solution-processed PEDOT:PSS-free inverted perovskite solar cells. *ACS Appl. Mater. Interfaces* **10**, 21466–21471 (2018).
33. Chi, D. et al. Composition and interface engineering for efficient and thermally stable Pb–Sn mixed low-bandgap perovskite solar cells. *Adv. Funct. Mater.* **28**, 1804603 (2018).
34. Jeng, J.-Y. et al. Nickel oxide electrode interlayer in CH₃NH₃PbI₃ perovskite/PCBM planar-heterojunction hybrid solar cells. *Adv. Mater.* **26**, 4107–4113 (2014).
35. You, J. et al. Improved air stability of perovskite solar cells via solution-processed metal oxide transport layers. *Nat. Nanotechnol.* **11**, 75–81 (2015).
36. Fang, Z., Xiao, K. & Tan, H. Low-temperature processed inorganic hole transport layer for efficient and stable mixed Pb–Sn low-bandgap perovskite solar cells. *Sci. Bull.* **64**, 1399 (2019).
37. Lee, S. J. et al. Reducing carrier density in formamidinium tin perovskites and its beneficial effects on stability and efficiency of perovskite solar cells. *ACS Energy Lett.* **3**, 46–53 (2017).
38. Diau, E. W.-G., Jokar, E. & Rameez, M. Strategies to improve performance and stability for tin-based perovskite solar cells. *ACS Energy Lett.* **4**, 1930–1937 (2019).
39. Lin, Q., Armin, A., Nagiri, R. C. R., Burn, P. L. & Meredith, P. Electro-optics of perovskite solar cells. *Nat. Photon.* **9**, 106–112 (2014).
40. Walsh, A. & Stranks, S. D. Taking control of ion transport in halide perovskite solar cells. *ACS Energy Lett.* **3**, 1983–1990 (2018).
41. Hauff, Evon Impedance spectroscopy for emerging photovoltaics. *J. Phys. Chem. C* **123**, 11329–11346 (2019).
42. Shi, J. et al. From ultrafast to ultraslow: charge-carrier dynamics of perovskite solar cells. *Joule* **2**, 879–901 (2018).
43. Zarazua, I. et al. Surface recombination and collection efficiency in perovskite solar cells from impedance analysis. *J. Phys. Chem. Lett.* **7**, 5105–5113 (2016).
44. Mahmood, K., Sarwar, S. & Mehran, M. T. Current status of electron transport layers in perovskite solar cells: materials and properties. *RSC Adv.* **7**, 17044–17062 (2017).
45. Brandt, R. E., Stevanović, V., Ginley, D. S. & Buonassisi, T. Identifying defect-tolerant semiconductors with high minority-carrier lifetimes: beyond hybrid lead halide perovskites. *MRS Commun.* **5**, 265–275 (2015).
46. Blum, V. et al. Ab initio molecular simulations with numeric atom-centered orbitals. *Comput. Phys. Commun.* **180**, 2175–2196 (2009).
47. Havu, V., Blum, V., Havu, P. & Scheffler, M. Efficient *O(N)* integration for all-electron electronic structure calculation using numeric basis functions. *J. Comput. Phys.* **228**, 8367–8379 (2009).
48. Ren, X. et al. Resolution-of-identity approach to Hartree–Fock, hybrid density functionals, RPA, MP2 and GW with numeric atom-centered orbital basis functions. *New J. Phys.* **14**, 053020 (2012).
49. Weston, L., Taylor, H., Krishnaswamy, K., Bjaalie, L. & Van de Walle, C. G. Accurate and efficient band-offset calculations from density functional theory. *Comput. Mater. Sci.* **151**, 174–180 (2018).
50. Li, C. et al. Ultrafast and broadband photodetectors based on a perovskite/organic bulk heterojunction for large-dynamic-range imaging. *Light Sci. Appl.* **9**, 31 (2020).
51. Zheng, T. et al. Polymer: fullerene bimolecular crystals for near-infrared spectroscopic photodetectors. *Adv. Mater.* **29**, 1702184 (2017).
52. Yao, Y. et al. Plastic near-infrared photodetectors utilizing low band gap polymer. *Adv. Mater.* **19**, 3979–3983 (2007).
53. Kim, J. Y. et al. Single-step fabrication of quantum funnels via centrifugal colloidal casting of nanoparticle films. *Nat. Commun.* **6**, 7772 (2015).
54. Wang, W. et al. Highly sensitive low-bandgap perovskite photodetectors with response from ultraviolet to the near-infrared region. *Adv. Funct. Mater.* **27**, 1703953 (2017).
55. Shen, L. et al. Integration of perovskite and polymer photoactive layers to produce ultrafast response, ultraviolet-to-near-infrared, sensitive photodetectors. *Mater. Horiz.* **4**, 242–248 (2017).
56. Clifford, J. P. et al. Fast, sensitive and spectrally tuneable colloidal-quantum-dot photodetectors. *Nat. Nanotechnol.* **4**, 40–44 (2009).

Acknowledgements

This work was supported by the Natural Sciences and Engineering Research Council (NSERC) Alexander Graham Bell Canada Graduate Scholarships (CGS-D), Materials for Enhanced Energy Technologies (MEET) scholarships and the NSERC Collaborative Research and Training Experience (CREATE) program (grant no. 466083). F.P.G.A. acknowledges funding from CEX2019-000910-S (MCIN/AEI/10.13039/501100011033), Fundació Cellex, Fundació Mir-Puig, Generalitat de Catalunya through CERCA.

Author contributions

A.M.N., F.P.G.A. and E.H.S. conceived the idea and designed the experiments. M.W. contributed to the initial fabrication and speed measurements. A.M.N. and M.V. modelled the device performance and also fabricated the devices. M.V. measured the EQE and dark current of the device. A.M.N. performed the TPC measurement and LiDAR demo. T.Z. performed the theoretical calculation for SnO_x energy level. E.H.S., S.H., M.I.S. and Y.H. provided advice. A.M.N., A.J., M.V., F.P.G.A. and E.H.S. composed the manuscript. All the authors discussed the results and commented on the manuscript.

Competing interests

The authors declare no competing interests.

Additional information

Extended data is available for this paper at <https://doi.org/10.1038/s41928-022-00799-7>.

Supplementary information The online version contains supplementary material available at <https://doi.org/10.1038/s41928-022-00799-7>.

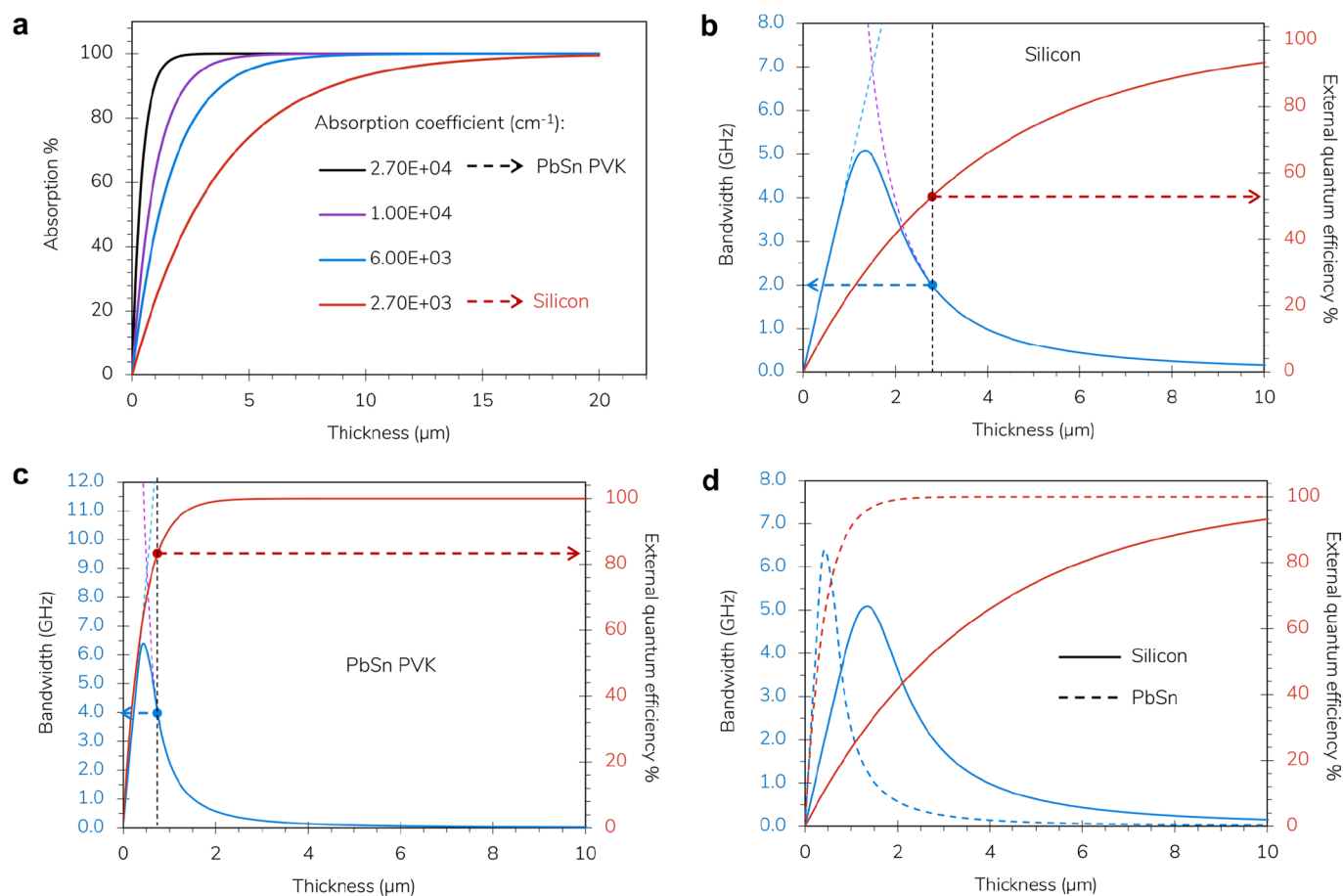
Correspondence and requests for materials should be addressed to Amin Morteza Najarian or Edward H. Sargent.

Peer review information *Nature Electronics* thanks the anonymous reviewers for their contribution to the peer review of this work.

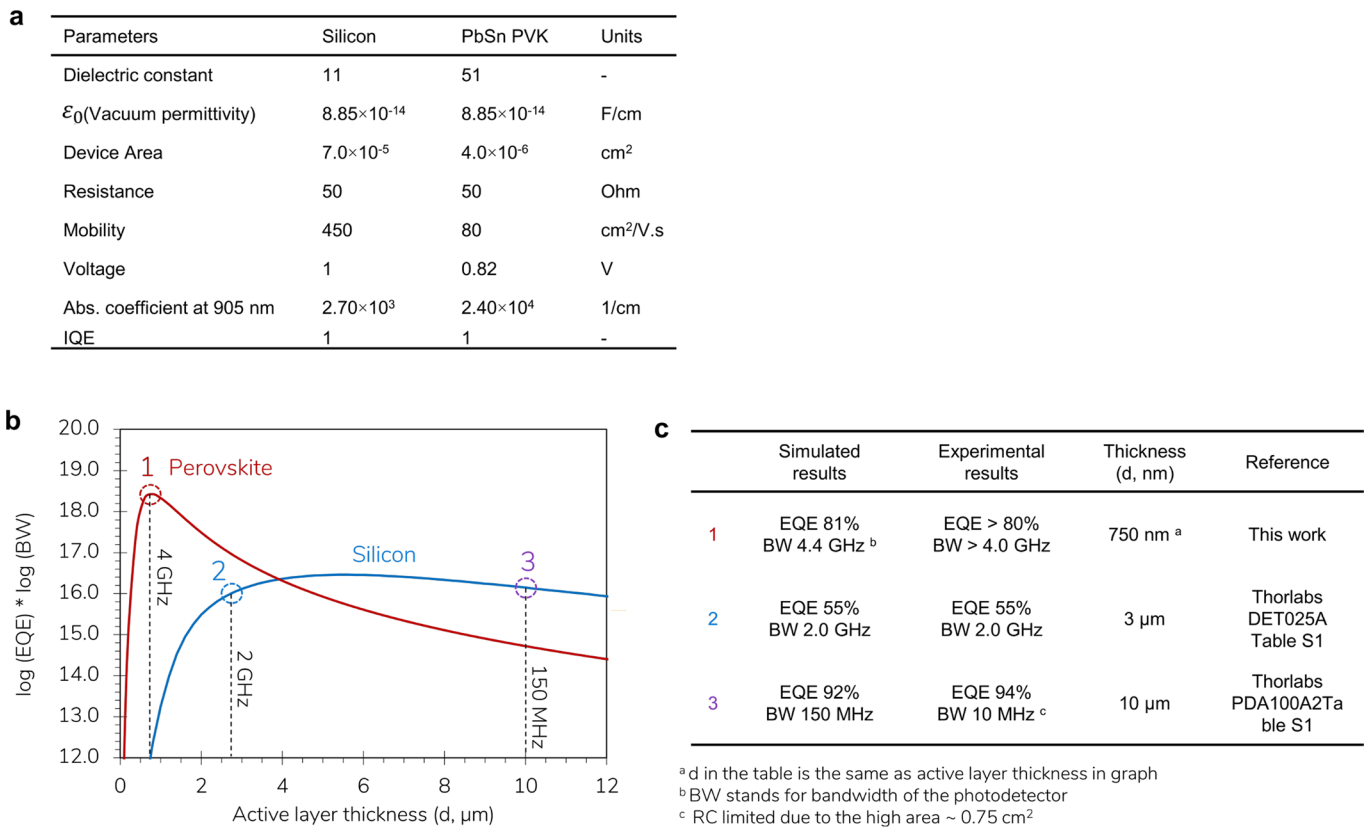
Reprints and permissions information is available at www.nature.com/reprints.

Publisher's note Springer Nature remains neutral with regard to jurisdictional claims in published maps and institutional affiliations.

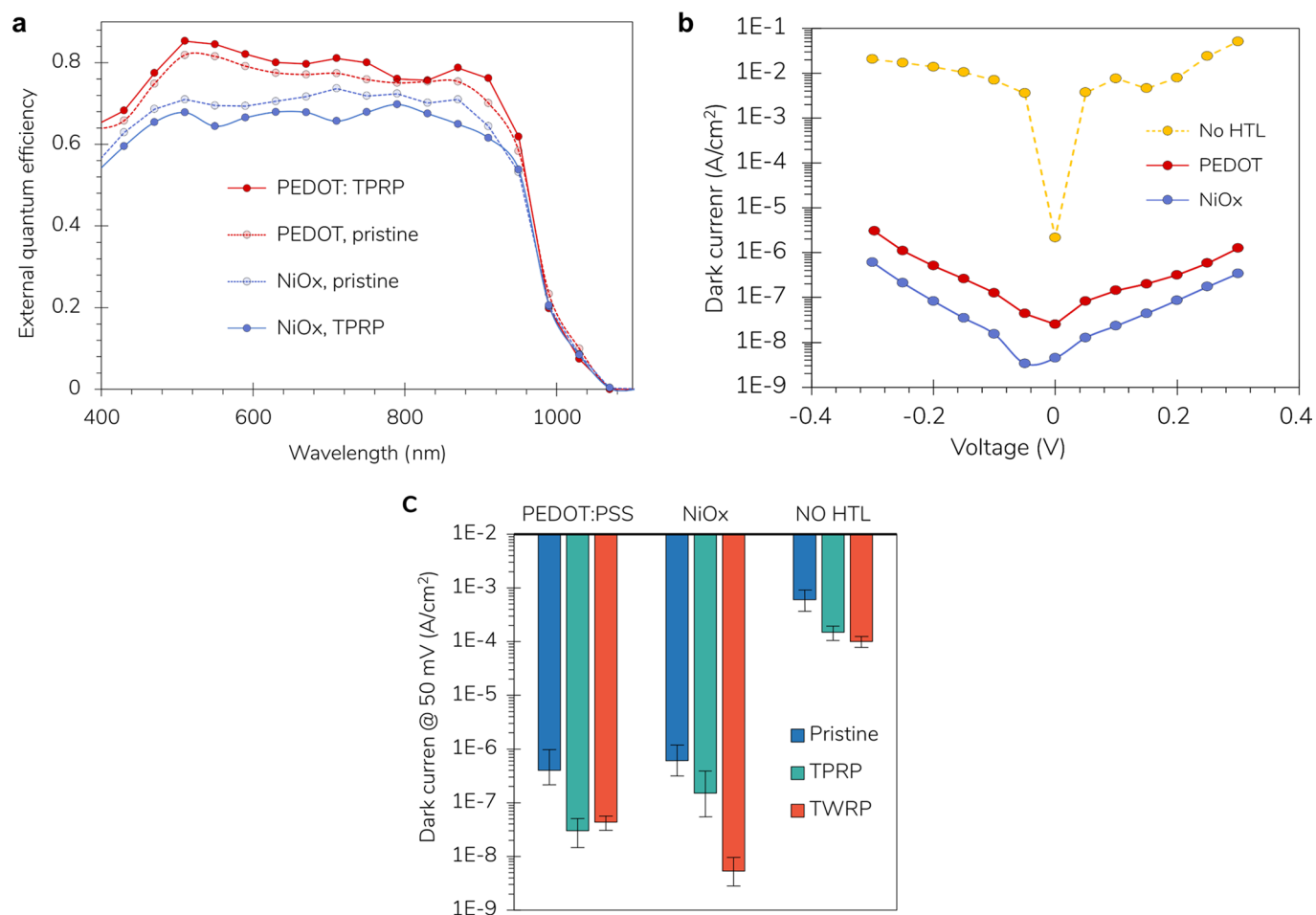
© The Author(s), under exclusive licence to Springer Nature Limited 2022



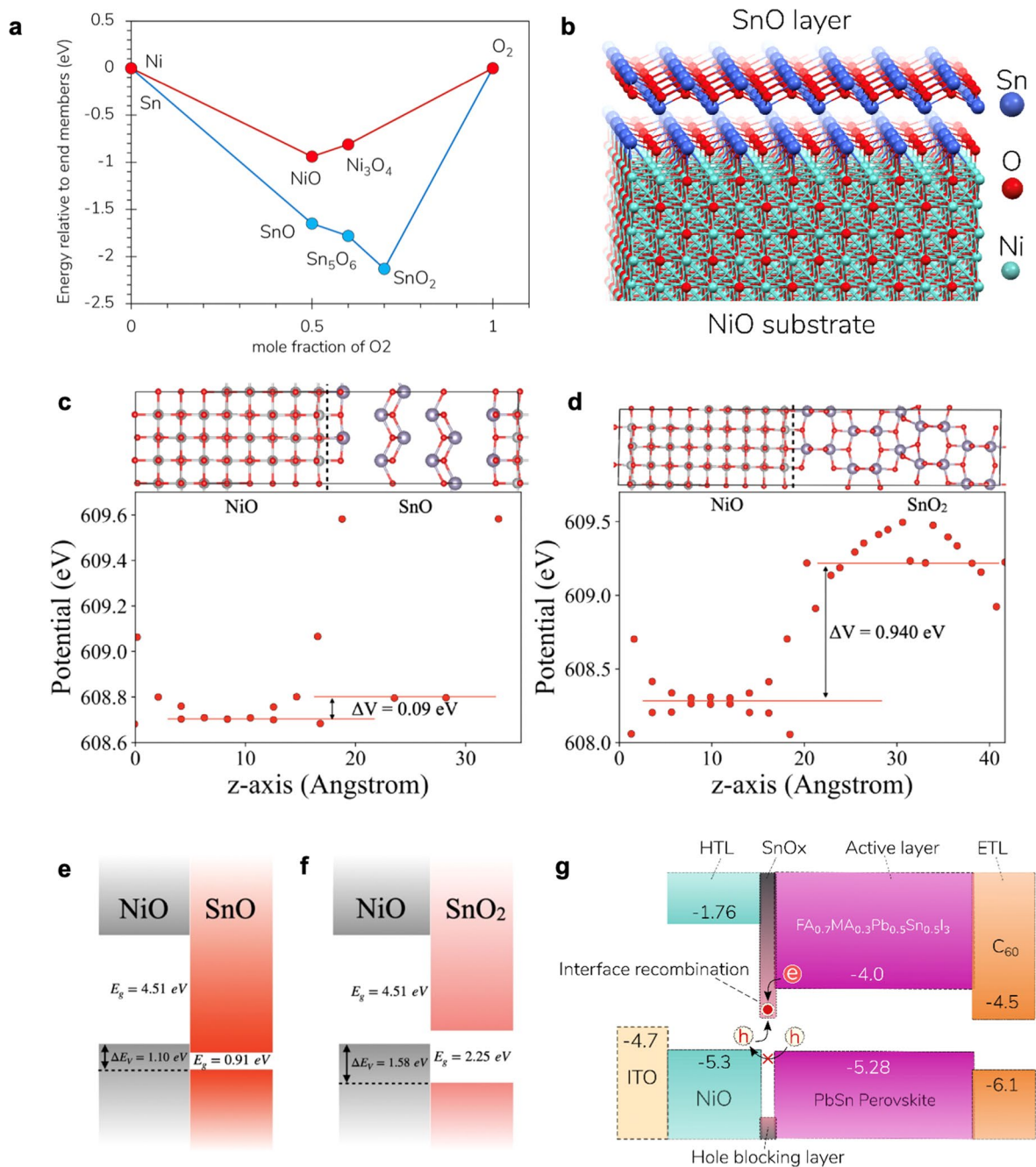
Extended Data Fig. 1 | Performance modeling of the photodetector. Equations are provided in Methods section. **a**, Percentage of absorbed light vs. thickness at indicated absorption coefficients. EQE and bandwidth of **b**, Silicon and **c**, PbSn perovskite vs. film thickness. **d**, Comparison of silicon and PbSn perovskite from the last two panels. Parameters used for the modeling are given in Extended Data Fig. 2a.



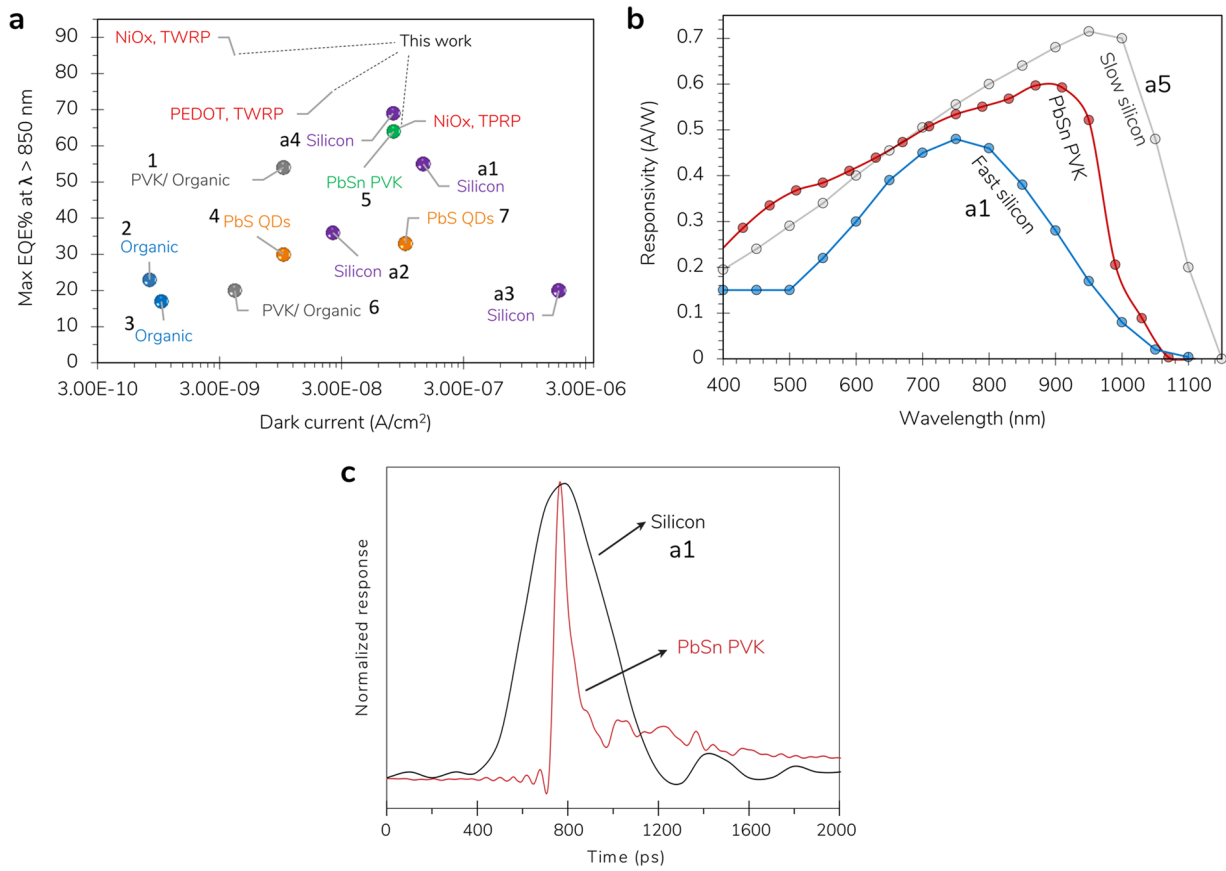
Extended Data Fig. 2 | Combined speed × efficiency characteristic of the photodetector. **a**, Parameters used in the modeling of PbSn and Silicon photodetectors. **b**, Combined speed × efficiency modeling of silicon and PbSn PVK. **c**, Comparison between estimated performance and actual devices.



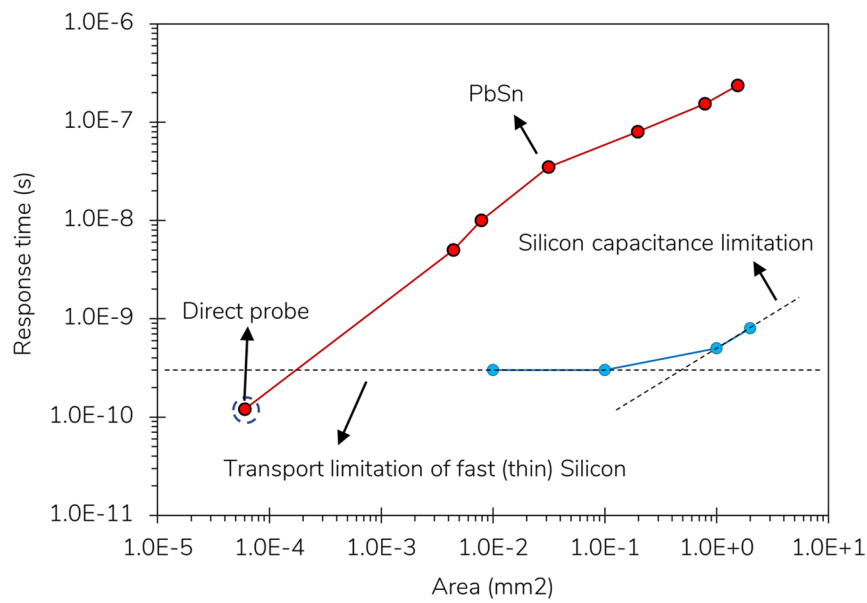
Extended Data Fig. 3 | Performance of NiO_x vs PEDOT:PSS HTL. **a**, EQE comparison between PEDOT:PSS and NiO_x using tin-powder reduced precursor (TPRP) strategy. **b**, Representative current density vs. voltage (*JV* curves) under the dark condition for the mentioned HTLs. Tin wire-reduced precursor strategy is used for all three shown cases. **c**, Comparison of dark current density at 50 mV for devices fabricated with PEDOT:PSS, NiO_x, and without HTL with different Sn reducing strategy.



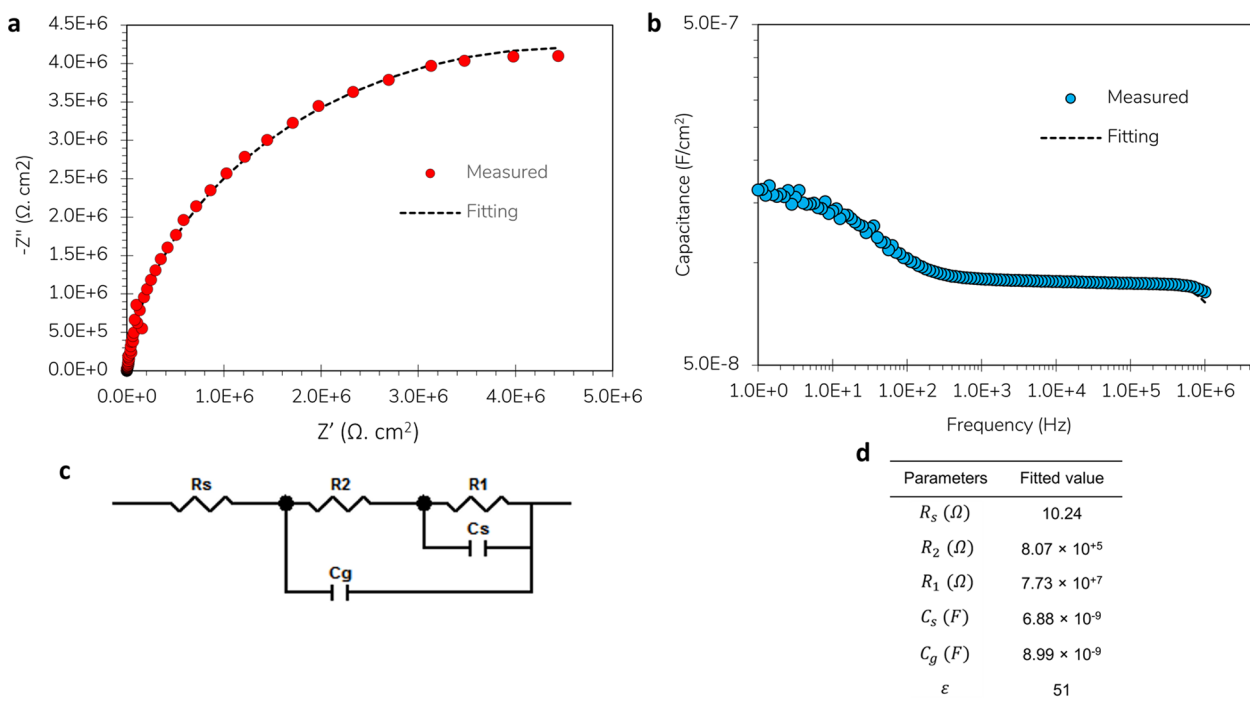
Extended Data Fig. 4 | Possibility of interfacial SnO_x formation. **a**, Diagram comparing the formation energy of different form of oxide for Ni and Sn. Electrostatic potential (in eV) at the cores of oxygen atoms along the longitudinal direction of the **b**, DFT simulated structure of formed SnO layer on top of NiO HTL. **c**, NiO/SnO (001) and **d**, NiO/SnO₂ (001) longitudinally lattice-matched supercell calculated by DFT-PBE within spin-polarized treatment for Ni. In each subplot, the top are the atomic structures of a (001)-oriented NiO/(SnO/SnO₂) superlattice; Ni atoms are shown in grey, Sn atoms are purple, and O atoms are red. Schematic plots of the band alignment for **e**, NiO/SnO and **f**, NiO/SnO₂ interface. The bandgap values are obtained according to a bulk calculation with HSE06 functional. **g**, Energy level diagram for different layers of fabricated devices, including SnO.



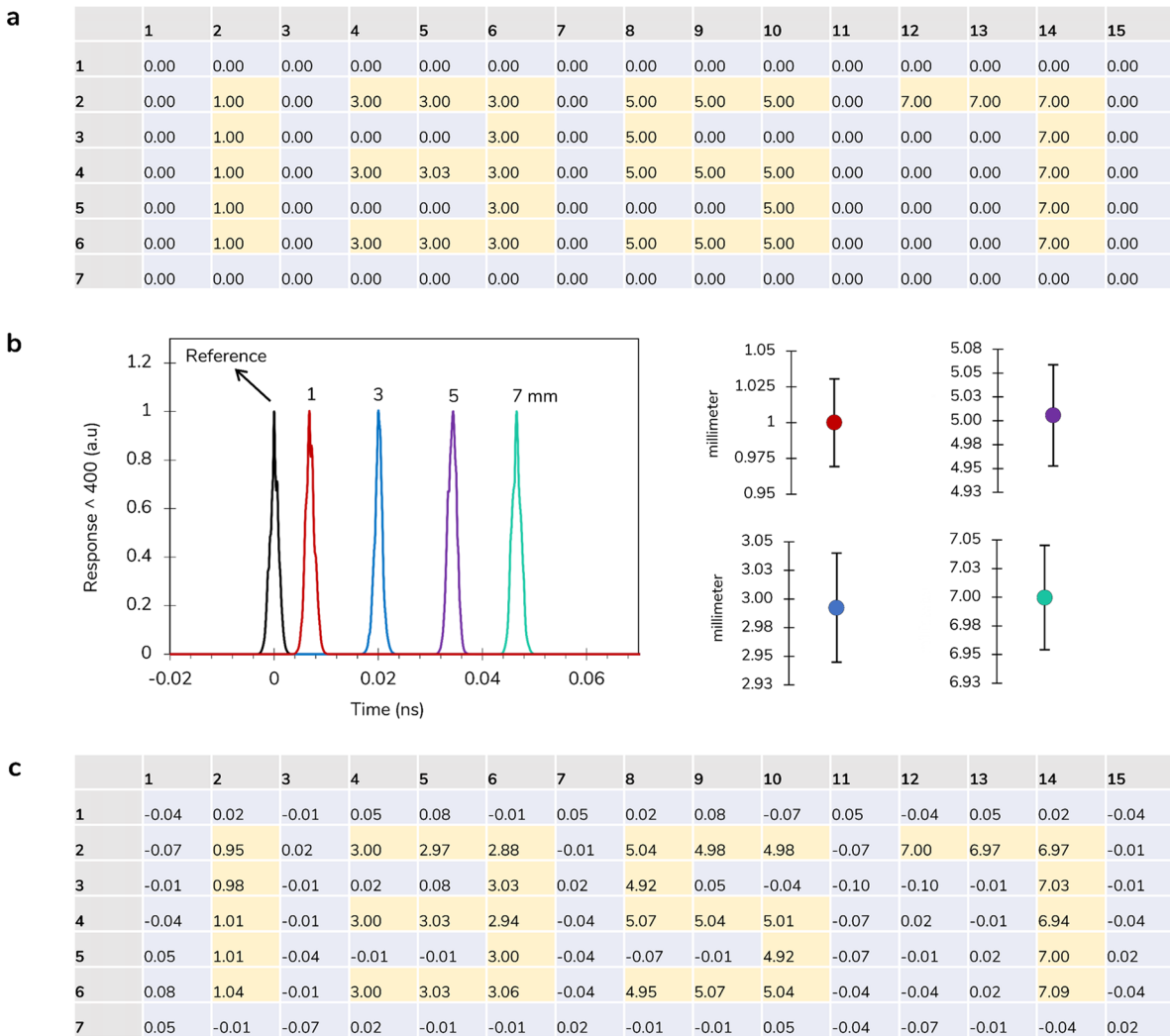
Extended Data Fig. 5 | Citation for the data used in the manuscript. a, Fig. 3a; **b**, Fig. 3b; **c**, Fig. 4c. The numbers shown in the Figure, refer to the raw number in Extended Data Tables 1 and 2.



Extended Data Fig. 6 | Geometrical capacitance effect in photodetectors time response. Measured fall time of the pixels is plotted vs. pixel area (mm²). The area for direct probe connection is estimated with the extension of the capacitance-limited regime. The area could be smaller than the estimated one. Area effect on response time of silicon photodetector is also compared with PbSn. Silicon below 0.1 mm² reaches the plateau, and further decrease in the area does not decrease the response time. This behaviour indicates that the relatively poor carrier mobility limits the speed of Si PIN PDs.



Extended Data Fig. 7 | Impedance measurement of the PbSn device. **a**, Impedance plot measured in the dark under short-circuit conditions. **b**, Capacitance spectra obtained under the same condition as panel a. Black lines correspond to fits. **c**, Modified Randles equivalent circuit used for the fitting with R_s , C_g , and C_s related to series resistance, geometrical capacitance, and interface accumulation capacitance and R_2 and R_1 as surface recombination resistance. **d**, Parameters obtained by fitting the impedance data with Randles equivalent circuit.



Extended Data Fig. 8 | Mapping of the distance using PbSn photodetector. **a**, The input for the mirror's position in the ToF setup shown in Fig. 5a for 105 individual measurements. The motorized stage controls the position of the mirror (distance in respect to the light source). The distance of zero is arbitrary, and it means that light is traveling the same distance as the reference pathway toward the InGaAs detector in the interferometer. **b**, Graph showing the response when the mirror has moved by 1.0, 3.0, 5.0, and 7.0 mm. For better visualization of peak positions, the response magnitude has multiplied by a power of 400. Averages and standard deviations of estimated depths based on the response time are shown on right side **c**, The output of the estimated distances using the peak position of PbSn photodetector response. The 3D visualization of these results is shown in Fig. 5d.

Extended Data Table 1 | Comparison of the solution-processed photodetectors

# code	HTL/Absorber /ETL	Max EQE% @ $\lambda > 850$ nm	Min dark current (A/cm ²) @ 50 mV	Response time			Stability ^d	Ref.
				Fall time ^b (ns)	Area (mm ²)	Bias (V)		
1	PTAA/ MAPbI ₃ / F8IC:PTB7-Th/ C ₆₀	54	1×10^{-8}	5.6	0.1	0	50% (storage, 120h)	50
2	MoO ₃ / PBTTT:PCBM/PEIE	23	8×10^{-10}	230	0.5	0	-	51
3	PEDOT:PSS/ PTT:PCBM	17	1×10^{-9}	62	1	0	-	52
4	MoO ₃ / PbS-QD/ TiO ₂	30 @ 0.5 V	1×10^{-8}	292	-	0	-	53
5	PEDOT:PSS/ (FASnI ₃) _{0.6} (MAPbI ₃) _{0.4} / C ₆₀	64 @ 0.2 V	8×10^{-8}	9100	3.8	0.2	96% (storage, 90days)	54
6	PTAA/ MAPbI ₃ / PDPPTDTP:PCBM	20 @ 0.2 V	4×10^{-9}	5	0.1	0.2	-	55
7	PbS-QD	33	1×10^{-7}	70	1.96	5	-	56
8	NiO _x / PbSn/ C60/ BCP/ Ag	85 ^a	5×10^{-9}	<0.2	<0.001	0	96% (continuous illumination, 10 hours)	This work

^aEQE and speed was measured on the same device. EQE was measured on the pixels with a area of 0.049 cm². Time response was measured for a range of pixel areas as it is shown in Extended Data Fig. 6. ^bFastest measured response times are listed. ^cThe effect of device area on response time is shown in extended data Fig. 6. Response times in the capacitance-limited region (larger pixel area) do not reflect the charge carrier mobility or speed of carrier transfer rate across the device, as these response times are governed by the capacitance and resistance of devices. ^dDetails of measurement conditions and more references for stability are listed in Supplementary Table 4.

Extended Data Table 2 | Comparison of commercial silicon photodetector

code No.	Company	Model	R (A/W) @ 850 nm	EQE @ 850 nm	Speed (GHz)	Rise time (ps)	Dark (A)	Diameter (mm)	Area (cm ²)	Current Density
a1	Thorlabs	DET025A	0.38	0.55	2.0	230	3.5×10^{-11}	2.5×10^{-4}	4.9×10^{-4}	1.4×10^{-7}
a2	Hamamatsu	S9055-01	0.25	0.36	2.0	250	2.0×10^{-12}	1.0×10^{-4}	7.8×10^{-5}	2.5×10^{-8}
a3	Newport	818-BB-20	0.14	0.20	1.0	350	1.1×10^{-10}	8.8×10^{-5}	6.1×10^{-5}	1.8×10^{-6}
a4	Newport	818-BB-21	0.47	0.69	1.2	300	1.0×10^{-10}	4.0×10^{-4}	1.3×10^{-3}	7.9×10^{-8}
a5	Thorlabs	PDA100A2	0.64	0.94	<0.01	30000>	$<1 \times 10^{-9}$	9.8	0.75	$<1.3 \times 10^{-9}$